STRUCTURAL BIOLOGY

Dynamics and mechanism of a light-driven chloride pump

Sandra Mous[1], Guillaume Gotthard[1,2], David Ehrenberg[3], Saumik Sen[4]†, Tobias Weinert[2], Philip J. M. Johnson[5], Daniel James[2]‡, Karol Nass[6], Antonia Furrer[2], Demet Kekilli[2]§, Pikyee Ma[2]¶, Steffen Brünle[2]#, Cecilia Maria Casadei[1,2], Isabelle Martiel[7], Florian Dworkowski[7], Dardan Gashi[2,6], Petr Skopintsev[2]**, Maximilian Wranik[2], Gregor Knopp[6], Ezequiel Panepucci[7], Valerie Panneels[2], Claudio Cirelli[6], Dmitry Ozerov[8], Gebhard F. X. Schertler[1,2], Meitian Wang[7], Chris Milne[6]††, Joerg Standfuss[2], Igor Schapiro[4], Joachim Heberle[3], Przemyslaw Nogly[1]*

Chloride transport by microbial rhodopsins is an essential process for which molecular details such as the mechanisms that convert light energy to drive ion pumping and ensure the unidirectionality of the transport have remained elusive. We combined time-resolved serial crystallography with time-resolved spectroscopy and multiscale simulations to elucidate the molecular mechanism of a chloride-pumping rhodopsin and the structural dynamics throughout the transport cycle. We traced transient anion-binding sites, obtained evidence for how light energy is used in the pumping mechanism, and identified steric and electrostatic molecular gates ensuring unidirectional transport. An interaction with the π-electron system of the retinal supports transient chloride ion binding across a major bottleneck in the transport pathway. These results allow us to propose key mechanistic features enabling finely controlled chloride transport across the cell membrane in this light-powered chloride ion pump.

Chloride transport is a fundamental process in biology, regulating osmotic pressure, cell growth, and membrane potential (*1*). In halophilic Archaea, inward halide-pumping rhodopsins (halorhodopsin; HR) from *Halobacterium salinarum* (*Hs*HR) and *Natromonas pharaonis* (*Np*HR) help to generate the membrane potential to produce ATP through the proton motive force, together with the outward proton-pumping bacteriorhodopsin (*2*–*4*). The role of halorhodopsin in marine bacteria, such as rhodopsin 3 from *Nonlabens marinus* (*Nm*HR), remains unclear, but it has been speculated that these chloride pumps are involved in producing ATP and maintaining the osmotic balance of the cell (*5*). Ion gradients are also involved in the generation and propagation of neuronal signals, which has enabled the application of these photoactive chloride-pumping rhodopsins as optogenetic tools in the control of neuronal activity (*6*). Chloride-pumping rhodopsins bind a retinal chromophore in all-*trans* configuration, which, upon photoisomerization, initiates the transport cycle (fig. S1) through a mechanism that is still not well understood. The main transport events can be described following a modified Jardetzky alternate access model (*7*) in which a high-affinity substrate-binding site is transformed into a low-affinity site with light-induced structural changes enabling access to the cytoplasmic release pathway (fig. S2).

The first structure of a halide-pumping rhodopsin from halophilic Archaea was reported 20 years ago (*8*), revealing a chloride-binding site close to the protonated Schiff base (PSB) of the retinal. However, it is essential to determine transient chloride-binding sites to decipher details of the ion transport mechanism. These remained elusive, except for one transient site that was identified in cryo-trapped photointermediate states of the archaeal halorhodopsins *Hs*HR (*9*) and *Np*HR (*10*). Recently, the resting structure of the chloride pump *Nm*HR from marine bacteria was published (*11*, *12*). Although the latter shares only 21% sequence identity with *Hs*HR and *Np*HR, it is conceivable that these structurally similar proteins may use comparable elements in their transport mechanism. Similarities are also evident in the photocycle. The classical bacteriorhodopsin photocycle is usually described by the following scheme: dark + hν → K→ L → M→ N → O → dark. Halorhodopsins do not display the M state intermediate, indicating the lack of a PSB deprotonation stage [for a detailed photocycle comparison, see fig. S3 (*13*–*17*)].

Understanding the molecular mechanism of ion transport requires a methodology with near-atomic spatial resolution and up to picosecond temporal resolution (*13*, *15*, *18*–*26*). Recent years have witnessed rapid development in the field of time-resolved serial femtosecond crystallography (TR-SFX) at x-ray free electron laser (XFEL) facilities with a similar strategy adapted to synchrotrons: time-resolved serial synchrotron crystallography (TR-SSX). The ability to photoactivate rhodopsins renders *Nm*HR an ideal target for time-resolved pump-probe experiments to elucidate the structural dynamics of chloride transport. The ion transport in halorhodopsin contrasts in charge and direction with the studied with TR-SFX bacteriorhodopsin (*13*, *23*, *25*) and the sodium-pumping rhodopsin *Krokinobacter eikastus* rhodopsin 2 [KR2 (*15*)], thus presenting an interesting opportunity for mechanistic comparison of transport strategies in nature.

In this work, we used an approach based on the detection of anomalous signals in the photostationary state using the serial crystallography method to identify transient anion-binding sites inside *Nm*HR. In addition, to provide a comprehensive view of the anion transport mechanism in *Nm*HR, structural intermediates from Δt = 10 ps until 50 ms were determined using a combination of TR-SFX and TR-SSX for resolving structural intermediates of the early and late photocycle, respectively. Our structural data were complemented with crystal spectroscopy and hybrid quantum mechanics/molecular mechanics (QM/MM) simulations. The time-resolved crystallography experiments allowed us to describe two molecular gates orchestrating the unidirectional chloride transport and analyze the mechanism of light energy utilization in transport initiation proceeding through an interaction of the retinal π-electron system with the chloride.

Results and discussion

Tracing the chloride transport pathway

A chloride-binding site named Cl^{351} was identified on the extracellular side of the retinal-binding pocket in the resting state of *Nm*HR (*11*, *12*) (fig. S4C). Chloride transport to the cytoplasm would thus require transfer across the retinal. The presence of such an early transport bottleneck ensures tight light control, enabling transport only upon photoactivation. The resting-state structure of *Nm*HR revealed three water cavities formed by conserved residues (fig. S4, A and B, and S5) that may be involved in the transport pathway. However, a prominent tunnel that would allow for the passage of the anion was not identified. Previous biochemical studies showed that *Nm*HR can transport (*5*) and bind bromide with a

[1]Institute of Molecular Biology and Biophysics, Department of Biology, ETH Zürich, Zürich, Switzerland. [2]Laboratory of Biomolecular Research, Biology and Chemistry Division, Paul Scherrer Institute, Villigen PSI, Switzerland. [3]Experimental Molecular Biophysics, Department of Physics, Freie Universität Berlin, Berlin, Germany. [4]Fritz Haber Center for Molecular Dynamics, Institute of Chemistry, The Hebrew University of Jerusalem, Jerusalem, Israel. [5]Laboratory of Nonlinear Optics, Photon Science Division, Paul Scherrer Institute, Villigen PSI, Switzerland. [6]Laboratory of Femtochemistry, Photon Science Division, Paul Scherrer Institute, Villigen PSI, Switzerland. [7]Laboratory for Macromolecules and Bioimaging, Photon Science Division, Paul Scherrer Institute, Villigen PSI, Switzerland. [8]Science IT, Paul Scherrer Institute, Villigen PSI, Switzerland.
*Corresponding author. Email: przemyslaw.nogly@mol.biol.ethz.ch
†Present address: Condensed Matter Theory Group, Laboratory for Theoretical and Computational Physics, Paul Scherrer Institute, CH-5232 Villigen PSI, Switzerland.
‡Present address: Department of Physics, Utah Valley University, Orem, UT 84058, USA.
§Present address: Celerion Switzerland AG, CH-8320 Fehraltorf, Switzerland.
¶Present address: Viromotix AG, CH-8952 Schlieren, Switzerland.
#Present address: Leiden Institute of Chemistry, Leiden University, 2333 CC Leiden, The Netherlands.
**Present address: California Institute for Quantitative Biosciences (QB3), University of California, Berkeley, Berkeley, CA, USA.
††Present address: European XFEL GmbH, 22869 Schenefeld, Germany.

similar affinity as chloride [Cl^-: K_d = 24 mM; Br^-: K_d = 10 mM (*17*)]. Furthermore, structural studies show that a bromide ion is coordinated by the retinal PSB in the resting-state Br^{351}-binding site (*11*). We have assumed that bromide can mimic the transport pathway of chloride ions. Therefore, to detect transient anion-binding sites across the protein, we replaced chloride with bromide, which can be localized by anomalous dispersion in x-ray diffraction. Bromide-soaked crystals were continuously illuminated with a 520-nm laser diode while being delivered for serial crystallographic data collection at the Swiss Light Source (*26*). Perpetually activating *Nm*HR within the crystals results in a photostationary state with a mixture of photocycle intermediates (Fig. 1B) and partial occupancies of possible anion-binding sites. However, the O spectroscopic intermediate was predominantly accumulated (fig. S6). Molecular replacement combined with single-wavelength anomalous dispersion enabled us to identify four intramolecular sites overlapping with internal water molecules (Fig. 1A, all scatterers listed in fig. S7, and tables S1 and S2): one corresponding to the resting state (Br^{351}), one in a hydrophilic cavity on the cytoplasmic half of the protein (Br^{353}), and two in hydrophilic cavities in the extracellular half of the protein (Br^{354} and Br^{355}).

To complement the steady-state experiments and to resolve the structural intermediates of the consecutive steps of transport, we collected time-resolved serial crystallography data. Time delays from picoseconds to microseconds were recorded at the SwissFEL X-ray Free Electron Laser (*27*) and complemented with millisecond data from the Swiss Light Source synchrotron (*26*) (fig. S8).

As discussed in the following sections, the time-resolved crystallography experiments allowed the temporal assignment of the transient binding sites identified in the photostationary state.

*Nm*HR photocycle in crystals

*Nm*HR was crystallized in a lipidic cubic phase that mimics the amphipathic environment of cellular membranes. Nevertheless, crystal contacts and crystallization conditions may influence protein kinetics in the crystalline state

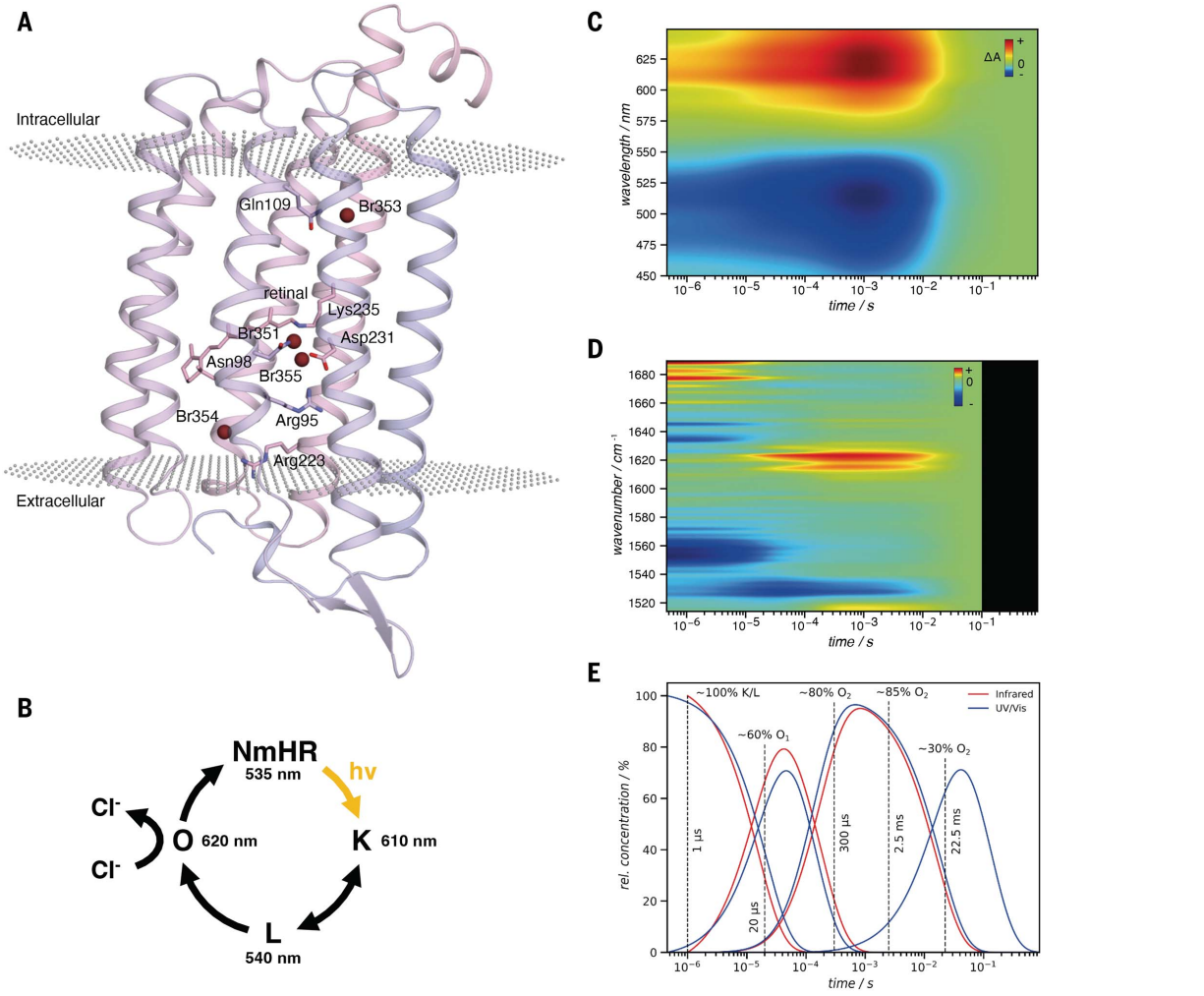

Fig. 1. Halide-binding sites and photocycle of *Nm*HR. (**A**) Ribbon model of *Nm*HR showing the overall secondary structure. Locations of bromide-binding sites, as determined by anomalous scattering, are shown as brown spheres. (**B**) Schematic representation of the *Nm*HR photocycle with the corresponding absorption maxima. (**C**) Two-dimensional representation of transient UV/Vis absorption experiments of *Nm*HR crystals after pulsed photoexcitation. Negative absorption changes (blue areas) correspond to the depletion of ground-state *Nm*HR and positive absorption (red areas) to the rise of intermediate states. (**D**) Kinetic data from time-resolved IR spectroscopy on the crystals. (**E**) Data in (C) and (D) have been subjected to global fit analysis by applying a model of sequential intermediate states. The analysis yielded the concentration profiles of the intermediate states, which were four states for the UV/Vis data (blue traces) and three states for the IR data (red traces), assigned to a mixture of the spectroscopic K/L state, the O_1 state, the O_2 state, and *Nm*HR′ (for which a signal was only observed in the UV/Vis data). The dashed vertical lines indicate the relative concentrations of intermediate states at delay times applied in the SFX experiments.

(*28*). We therefore probed the rise and decay of spectroscopic states (Fig. 1B) in crystals by time-resolved absorption spectroscopy in the infrared (IR) and in the ultraviolet/visible (UV/Vis) region (Fig. 1, C and D). In the nanoseconds to early microseconds, we observed a mixture of K (with λ_{max} at 610 nm) and L intermediates (with λ_{max} at 540 nm; table S3). The L intermediate decays into a red-shifted O intermediate (λ_{max} at 610 nm), which is predominant in the late microseconds until milliseconds (Fig. 1E). The photocycle of *Nm*HR probed in solution (*17*) indicated the rise of the early O_1 to be accompanied by chloride release and the decay of the subsequent O_2 state to be limited by chloride uptake. Compared with *Nm*HR in solution, the kinetics in the crystalline state are slightly altered with a faster decay rate of the spectroscopic intermediates up to the O_1 state and a slower decay rate of the O_2 state. These changes, however, can also be attributed to an increased chloride concentration (*17*).

*Nm*HR activation

Light-driven ion transport by microbial rhodopsins is initiated by the all-*trans* to 13-*cis* photoisomerization of the retinal chromophore. Time-resolved difference Fourier maps ($F_{o(10ps)} - F_{o(dark)}$) of our fastest TR-SFX time delay at Δt = 10 ps show that the retinal has isomerized (Fig. 2A and fig. S9). Structural refinement results in a nearly planar 13-*cis* configuration, however, the chromophore is tilted by 17° compared with the all-*trans*-retinal of the resting state (fig. S10, A

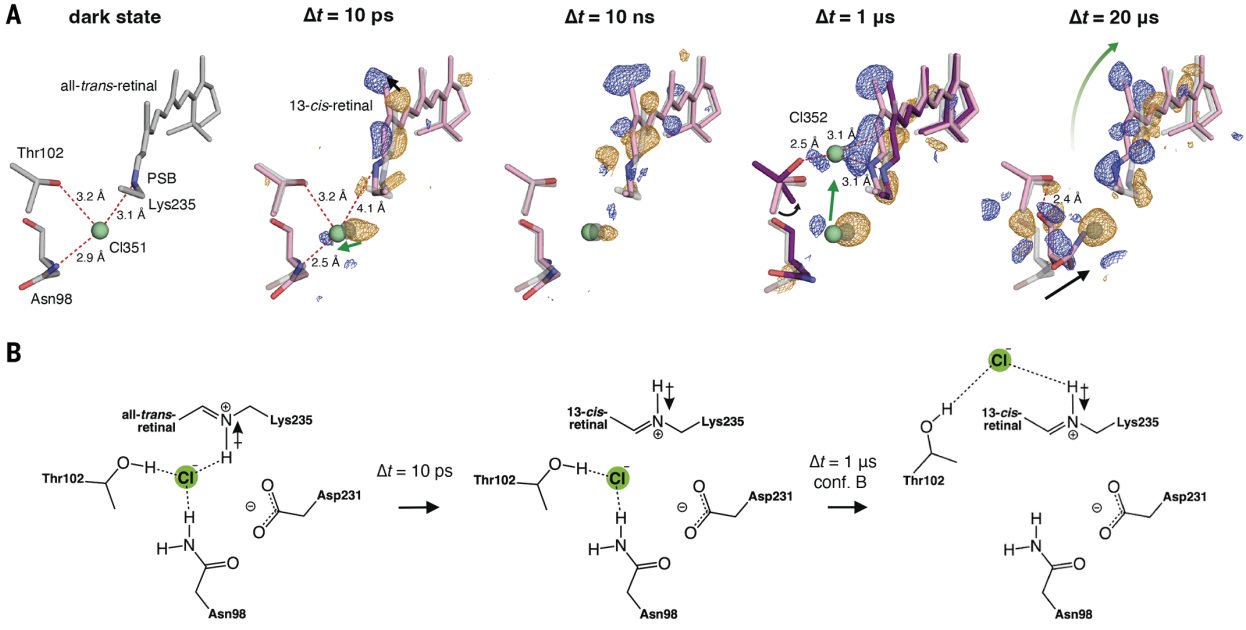

D

Structure	State	QM ΔE (nm)	Spectroscopic λ_{max} (nm)
Dark	Dark	510	535
10 ps	K	545	610
1 µs (conf. A)		552	
1 µs (conf. B)	L	514	540
20 µs	O_1	607	610
22.5 ms	O_2	591	620

Fig. 2. *Nm*HR activation and initiation of transport. (**A**) Chloride ion–binding site in the resting state and its evolution in the early active states. In the presence of photoisomerized retinal at Δt = 10 ps, when the spectroscopic K intermediate is accumulated, the Cl^{351} is shifted away from the PSB. At Δt = 1 µs, when a mixture of the K and L spectroscopic intermediates is accumulated, an additional Cl^{352}-binding site forms in the proximity of the PSB. Difference Fourier electron density ($F_{light} - F_{dark}$) contoured at 3.0 σ is shown as a blue (positive) mesh and a golden (negative) mesh. The corresponding extrapolated electron density maps can be found in figs. S11 and S12. The chloride ion is depicted as green sphere; the C atom sticks are colored gray (resting state) and pink (active states; Δt = 1 µs conformation B in dark purple). At Δt = 20 µs, when the O_1 spectroscopic intermediate is accumulated, the anion has passed over the retinal chromophore and the resting-state Cl^{351}-binding site has been depleted. (**B**) Schematic overview of the PSB flipping dipole (Δt = 10 ps), dragging the chloride over the retinal chromophore (Δt = 1 µs). (**C**) Molecular electrostatic potential surface of the retinal chromophore (with the nitrogen of the PSB shown as a blue sphere) and Cl^{352} (green sphere) of the 1-µs intermediate. The isocontour value of the surface is 0.005 e $Bohr^{-3}$. Blue and yellow colors correspond to regions of positive and negative electrostatic potential (in atomic units), respectively. Comparison with absent chloride is provided in fig. S15. (**D**) Absorption maxima of the resting state and the photocycle intermediates (excitation energy Δ*E*, in nanometers) as determined by QM/MM simulations and UV/Vis spectroscopy. The calculated values are consistently blue shifted, including the reference resting state. More details can be found in tables S6 and S7.

to C). The C20 methyl group of the isomerized retinal pushes against Trp^{201}, shifting it away by 0.4 Å. Trp^{99} shifts by 0.3 Å toward 13-*cis*-retinal, filling in the newly created space (fig. S11). The geometry of 13-*cis*-retinal resembles more closely that observed for sodium-pumping rhodopsin KR2 than that of bacteriorhodopsin (fig. S10D).

The PSB changes its orientation upon retinal isomerization. In the resting state, the proton of the PSB points toward the extracellular side and forms an H bond with Cl^{351} (Cl^{351}-PSB distance: 3.1 Å; Fig. 2, A and B). At Δt = 10 ps, the PSB flips, with its proton pointing toward the cytoplasm. Cl^{351} shifts away from the PSB, increasing the distance to 4.1 Å and breaking the H bond between the anion and the PSB, resulting in a destabilization of this binding site. Our QM/MM simulations indicate that 28.2 kcal mol^{-1} of energy is stored upon charge separation between the PSB and Cl^{351} at Δt = 10 ps. This energy corresponds to more than half of a green light photon (530 nm or 53.9 kcal mol^{-1}) to drive the subsequent reactions. Here, the stored energy is attributed to the photon energy that remains in the protein after the isomerization and subsequent return to the ground state. It is calculated as the difference between the resting state of *Nm*HR and the K intermediate.

A recent study complements our results, describing the ultrafast structural changes in *Nm*HR preceding chloride transport, including the retinal geometry evolution during the isomerization (*29*). Our 10-ps time delay provides a single time point overlap with the previous study, which shows overall agreement of the early structural changes.

First step of chloride transport

Upon depletion of the Cl^{351} site observed at Δt = 1 µs (Fig. 2A), we noted a positive difference density between the retinal PSB and Thr^{102}. We modeled it as chloride Cl^{352} in an alternate position to the still partially occupied Cl^{351} site (fig. S12). The partially formed Cl^{352}-binding site is stabilized by interactions with the retinal PSB (3.1 Å to Nζ), the π system (3.1 Å to C14 and C15 of the retinal), and the newly adopted 80° rotamer of Thr^{102} (2.5 Å to Oγ). We analyzed these interactions using quantum-chemical calculations and found that the stabilization is dominated by the electrostatic component between chloride and PSB (table S4). In addition, we have found a contribution from the C14–C15=N fragment of the retinal (fig. S13 and table S5). We identified an anion-π interaction between the conjugated π system of the retinal and Cl^{352} in which the negative charge of the anion polarizes the π-electron density of the chromophore (fig. S14). The polarization resembles the common interaction between anions and π electrons of aromatic rings (*30*–*35*). The polarization effect of the anion is also evident from the electrostatic potential maps of the retinal PSB in the presence of the chloride anion, with a negative potential extending up to the β-ionone ring of the retinal (Fig. 2C and fig. S15). Further validation stems from the calculated QM/MM excitation energy, which is in quantitative agreement with the experimental counterpart obtained from spectroscopy (Fig. 2D and tables S6 and S7). The red shift of the 1-µs intermediate with the anion in the Cl^{352}-binding site with respect to the resting state is 4 nm for the QM/MM simulation and 5 nm for the spectroscopic measurement. By contrast, when Cl^{352} is omitted or replaced by a water molecule, the computed shift is 164 or 187 nm, respectively.

On the basis of the archaeal *Hs*HR resting-state structure (*8*), it was hypothesized that the anion could be "dragged" by the moving PSB, but the passage across the retinal remained unknown. Our *Nm*HR data provide experimental evidence that, upon charge separation between photoisomerized retinal and Cl^{351} (leading to 28.2 kcal mol^{-1} of stored energy), the anion follows the PSB in microseconds, creating a pathway between the retinal and helix C. The identified anion-π interaction appears to be an essential step in the transport process. The first step of the chloride transport brings the anion 4.0 Å closer toward the cytoplasm.

Steric molecular gate

In the resting state, helix C exhibits a kink next to Cl^{351} [Fig. 3, B and C (*36*)]. Upon depletion of Cl^{351}, the kink on helix C relaxes from 38° ± 6° in the resting state to 22° ± 7° in the structure at Δt = 20 µs after light excitation. The kink relaxes even further, reaching a minimum angle of 16° ± 7° at Δt = 2.5 ms. A shift of helix C was also observed in active states of the homologous sodium-pumping rhodopsin KR2 (*15*). However, the observed changes do not lead to kink formation (fig. S16). We may infer

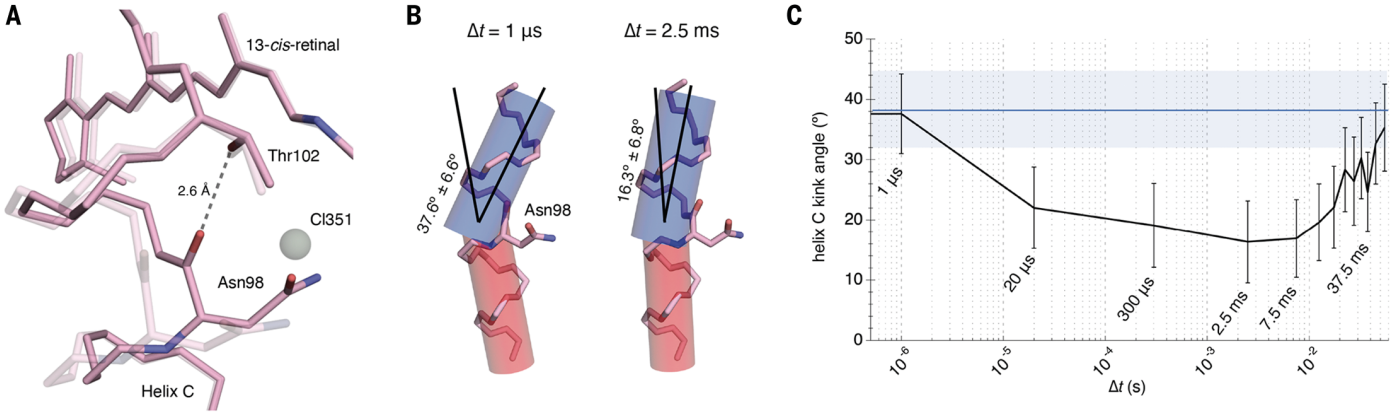

Fig. 3. Steric gate prevents chloride backflow. (**A**) Straightening of helix C at Δt = 20 µs to 7.5 ms, during which the spectroscopic O intermediates are accumulated, allows Asn^{98} to enter the resting-state chloride-binding site (intermediate Δt = 1 µs conformation A with the Cl^{351}-binding site shown in gray, intermediate Δt = 2.5 ms with a straightened helix C shown as pink sticks). The straightening of helix C is stabilized by the formation of a hydrogen bond between the backbone carbonyl group of Asn^{98} and the Thr^{102} side chain, shown by dashed lines with the distance measured in angstroms. (**B**) Two cylinders are fitted, from Asn^{92} to Asn^{98} and from Asn^{98} to Pro^{104}, from which the kink angle at Asn^{98} can be calculated (*36*). The fitted cylinders and calculated angle are shown for the Δt = 1 µs and Δt = 2.5 ms. (**C**) Change in the helix C kink angle over time, calculated using KinkFinder (*36*). One should consider that the apparent linear motion of the helix may be a result of changes in the populations of the intermediates. Error bars indicate the heuristically determined 95% confidence interval of the calculated kink angle (*36*). The blue line indicates the kink angle determined for the resting-state structure of 38.1°, with an estimated error of ± 6.3° represented in light blue.

that an intermediate state with sodium captured between retinal and helix C could lead to similar kink formation in KR2. In *Nm*HR, the relaxation of the kink moves the side chain of Asn^{98} into the chloride-free Cl^{351} site. This movement is rationalized as a sterically closing molecular gate preventing reverse flow of chloride. The Asn^{98} side chain, while replacing Cl^{351}, interacts only with the waters Wat^{484} (3.1 Å) and Wat^{407} (3.5 Å). Additional stabilization of this closed steric molecular gate is achieved by a new H bond between Thr^{102} and the carbonyl group of the Asn^{98} backbone (Fig. 3A), which seals the gate. Thr^{102}, which is part of the conserved NTQ motif defining the rhodopsin family to which *Nm*HR belongs (fig. S5), seems to play multiple roles in the early transport stages. In the resting state, it coordinates Cl^{351}, whereas at Δt = 1 µs, the Thr^{102} side chain assists in transferring the chloride to the Cl^{352} position by rotamerization. Finally, Thr^{102} seals the molecular gate, preventing chloride backflow from Δt = 20 µs once the anion is on its way toward the cytoplasm. The equivalent residue in sodium-pumping rhodopsin KR2 is Asp^{116}, which provides an electrostatic driving force for the cation and neutralizes the positive charge of the PSB (*15*), demonstrating substantial evolutionary adaptation of rhodopsins to different substrates.

Chloride release through Gln^{109} of the NTQ motif

At Δt = 20 µs, the Cl^{351}- and Cl^{352}-binding sites are depleted, and the Cl^{353} may emerge above the retinal by replacing Wat^{485}, which adds another 14 Å distance toward the cytoplasm on the transport pathway (Fig. 4A). The proposed transient Cl^{353}-binding site is characterized by a positive peak in $F_{o(20\mu s)} - F_{o(dark)}$ and displays an anomalous signal in the Br-soaked 13.7 keV photostationary SSX data (Fig. 1A). It should be noted that the anomalous difference density peak for the transient Cl^{353}-binding site is of limited strength (table S1 and fig. S7), likely because of the low occupancy of the transient binding site in the photostationary state. The Cl^{353}-binding site is accessed through Wat^{401} and Wat^{402} and formed by Gln^{109} of the conserved NTQ motif, Ser^{54} and Thr^{243} (Fig. 4A). We also observed a weak anomalous signal between Wat^{402} and Leu^{106} in the photostationary data (table S1). However, the site could not be modeled in our TR-SFX data. A conformational change of the residue corresponding to Leu^{106} (Ile^{134}) is needed to form a transient chloride-binding site in the *Np*HR structure of the N intermediate (*10*).

Gln^{109} of *Nm*HR is found at a strategic position for ion pumps. The equivalent residue of outward proton-pumping bacteriorhodopsin is Asp^{96}, which is the internal proton donor to the retinal Schiff base (*26*). In KR2, the equivalent residue is Gln^{123}, which is involved in the outward transport of sodium (*15*). These analogies suggest that pumping rhodopsins share sections of the transport pathway despite the different charge and size of the translocated ion and even in cases of opposite ion flow.

In the final stage, chloride is possibly released through the Wat^{482}-binding site on the surface, which is formed at Δt = 300 µs and within 8 Å from Cl^{353} (Fig. 4, B to D). It is accompanied by ordering of Thr^{51} and a rotameric change of Ser^{40}, both pointing toward Wat^{482}.

Chloride uptake

*Nm*HR appears to form an electric dipole (Fig. 5A) with the extracellular surface of predominantly negative charge and the cytoplasmic surface of predominantly positive charge. The resulting dipole moment presents an additional driving force for charge transport across the cell membrane, rendering directionality to those transitions that rely on passive anion diffusion.

The net negative charge on the extracellular solvent accessible surface creates a barrier for anion uptake (Fig. 5A), the exception being a water cavity enclosed by Asn^{3} (Fig. 5B). The anion entry into this cavity is driven by the positive charge of conserved Arg^{223}. We identified an anomalous site in the photostationary SSX data and a positive peak in the $F_{o(20\mu s)} - F_{o(dark)}$ map of the TR-SFX experiments, which we modeled as Cl^{354} (Fig. 1A and fig. S17). The latter is coordinated by Arg^{223}, Tyr^{96}, Wat^{403}, and Wat^{404}.

Passing of the chloride further toward the retinal is facilitated by the positive charge of the conserved Arg^{95}, likely through Wat^{429} (fig. S18A). To enter another water cavity consisting of Wat^{409} and Wat^{416} (from Δt = 1 µs, additionally Wat^{481}; fig. S19), the anion needs to pass Gln^{68}, where we observed a rotamer change only

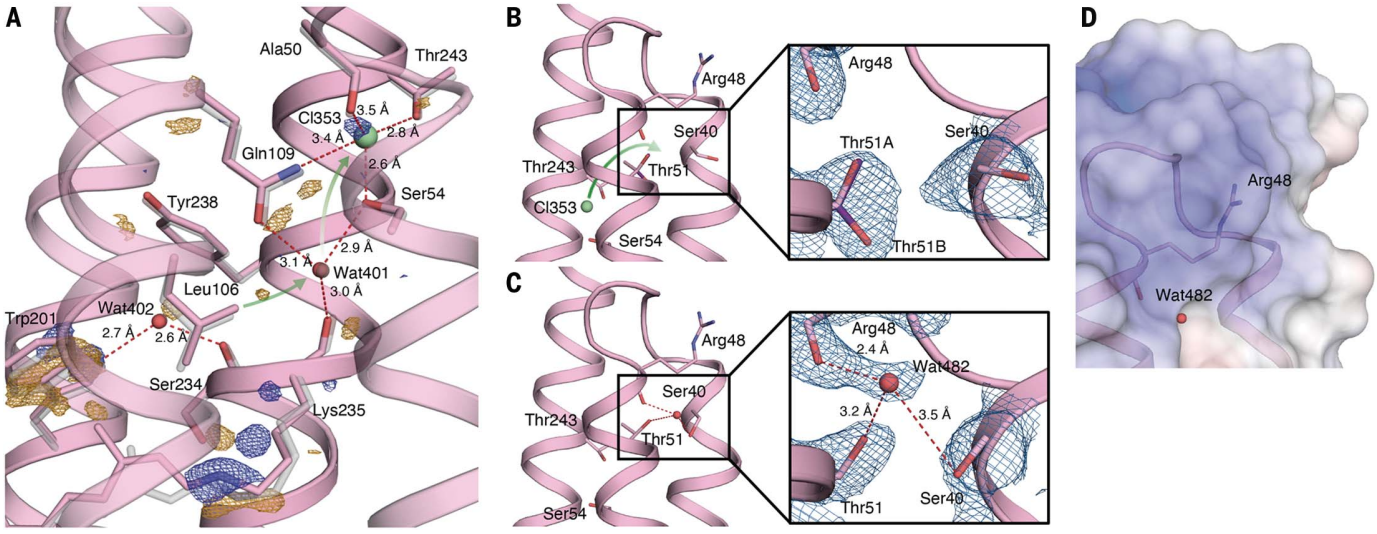

Fig. 4. Chloride transport and release. (**A**) A new chloride-binding site is identified after the anion is transferred over the retinal chromophore in the light-activated intermediate at Δt = 20 µs. Dashed lines indicate hydrogen-bonding interactions in the Cl^{353}-binding pocket with measurements in angstroms. Difference Fourier electron density [$F_{obs(20\ \mu s)} - F_{obs(dark)}$] contoured at 3.0 σ is shown as a blue (positive) mesh and a golden (negative) mesh. (**B**) Exit site at Δt = 20 µs. Conformation B of the Thr^{51} side chain is shown as purple sticks. The panel on the right shows a magnified view of the exit site with the extrapolated electron density ($2F_{ex} - F_{calc}$) as a blue mesh at 1.0 σ (carved at 1.8 Å from the side chains). (**C**) At Δt = 300 µs, the residue Ser^{40} changes conformation, whereas Thr^{51} adopts a single conformation to bind Wat^{482} (shown as a red sphere), which is only observed from Δt = 300 µs to 2.5 ms. At the same time, Cl^{353} and Wat^{485} are both absent at Δt = 300 µs. (**D**) Mapping the electrostatic potential (at ± 5 kT/e) on the solvent-accessible surface shows that the exit site is surrounded by a positive electrostatic potential.

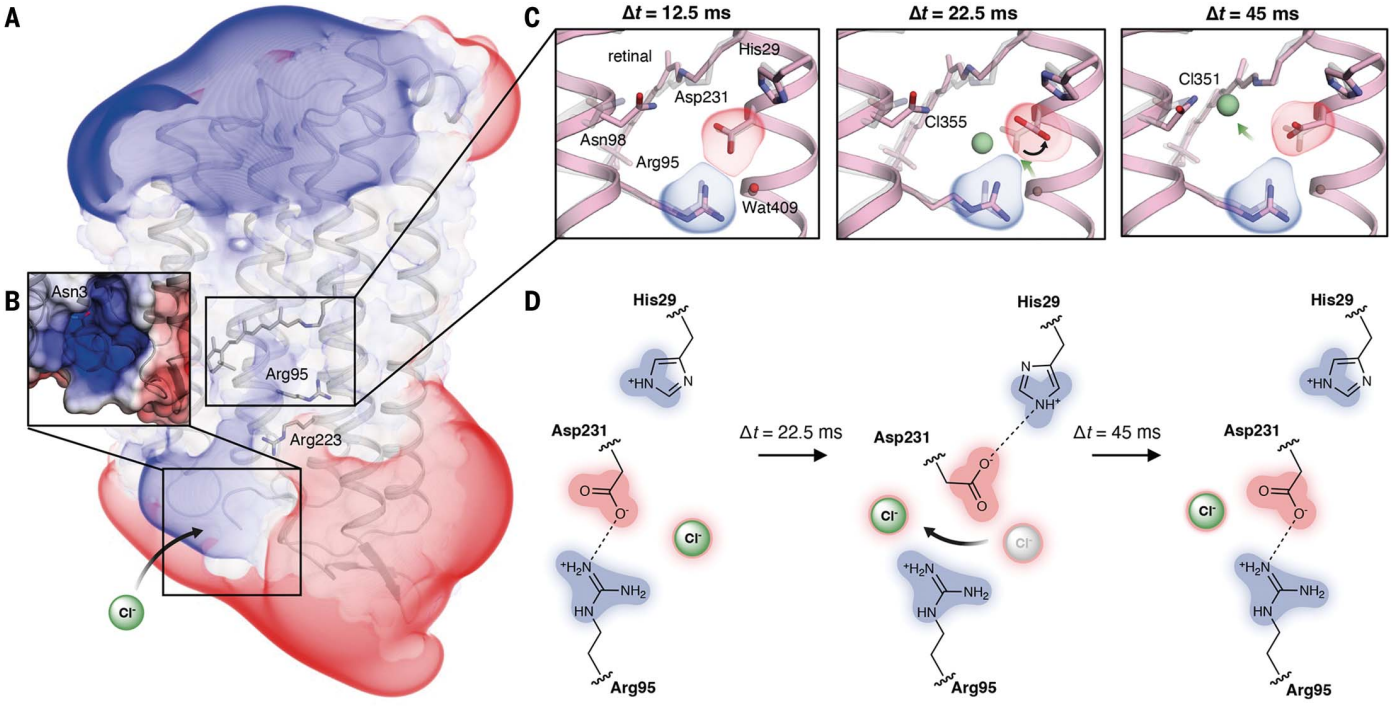

Fig. 5. Chloride uptake and electrostatic gate. (**A**) Ribbon model of *Nm*HR with surface electrostatics shown as an electrostatic potential isocontour at ±1 kT/e, with positive potential shown in blue and negative in red. (**B**) Solvent-accessible surface near the proposed chloride entrance site, with the electrostatic potential projected on the surface at ±3 kT/e. (**C**) Evolution of the accessibility to the retinal-binding pocket at Δt = 12.5 to 45 ms. The light-activated conformations are shown as light pink sticks overlaid on the resting-state structure shown as transparent gray sticks. The electrostatic potential isocontour at ±3 kT/e is shown around the Arg^{95} and Asp^{231} side chains. See fig. S20 for the corresponding electron densities. (**D**) Schematic representation of the electrostatic gate. As the chloride ion approaches residues Asp^{231} and Arg^{95} (step 1), the charge interaction between the residues is shielded, allowing Asp^{231} to interact with His^{29} instead (step 2). This creates a pathway for chloride to proceed toward the resting-state binding site (step 3).

at Δt = 12.5 ms (fig. S18B). Once the halide diffuses into the Wat^{409} position, the transport pathway is occluded by Asp^{231} (Fig. 5C and fig. S20).

Electrostatic gate enables recharging of the resting state

We calculated the excitation energy for different protonation states of Asp^{231} using hybrid QM/MM simulations to determine the form in which it is present. Only the anionic form of Asp^{231} results in the excitation energy consistent with the experimental value (table S8). Along with an interaction distance of 2.9 Å, it supports the presence of a salt bridge between Asp^{231} and Arg^{95}.

We propose that after diffusion into the Wat^{409} position, the halide interferes with the electrostatic attraction between Arg^{95} and Asp^{231} (Fig. 5C). We observed that the conformation of the side chain of Asp^{231} rotates from Δt = 22.5 to 37.5 ms, thereby interacting with the nearby His^{29} instead of Arg^{95} (Fig. 5, C and D). This opens the electrostatic gate and creates a pathway for the halide to the Cl^{355}-binding site, a convenient position for recharging of the Cl^{351} site 4 Å away. Before recovery of the resting state, the electrostatic gate closes again, preventing anion leakage back into the bulk solvent. In this way, the electrostatic gate ensures vectorial transport.

From Δt = 12.5 ms, the kink angle in helix C increases again (likely due to a shift in the populations of intermediates) until ~Δt = 45 ms, where helix C resembles the resting-state conformation (Fig. 3C). With the shift of helix C, the side chain of Asn^{98} also leaves the Cl^{351} site, and the retinal isomerizes back to all-*trans* configuration. It is plausible that the chloride pushes the side chain of Asn^{98} aside and breaks the steric gate seal driven by the energy gained from a strong electrostatic interaction with PSB.

Conclusions

We have traced several possible transient anion-binding sites buried inside *Nm*HR, allowing us to propose the chloride transport pathway (summarized in fig. S21 and movie S1). The time-resolved experiments enabled us to describe in atomic detail how the photonic energy absorbed by the retinal is stored in the form of charge separation between the isomerized retinal and its chloride counterion. In the early microseconds after protein activation, this excess energy drives the very first step of anion transport through an anion-π interaction. Comparing our results with the insights from previous TR-SFX studies of light-driven ion pumps (*13*, *15*), it becomes clear that rhodopsin pumps with different substrate affinities adopt diverse strategies to overcome the retinal bottleneck in ion transport. Whereas in bacteriorhodopsin and KR2, deprotonation of the Schiff base by the counterion (Asp^{85} and Asp^{116}, respectively) is required for successful transport, in *Nm*HR, no residue side chain acts as the proton acceptor, and the positively charged PSB drives the transfer of the anion over the chromophore.

In the steps after the initiation of anion transport, we propose that the steric molecular gate closes over the original anion-binding site accompanied by relaxation of helix C, which finally prevents a backflow. Anion release in the late microseconds is diffusion driven and assisted by the macroscopic dipole moment across the membrane created by the negative extracellular and positive cytoplasmic surface charges. The exit side to cytoplasm that we propose in this work aligns with the suggested ion selectivity filter in KR2 (*37*, *38*).

On the extracellular side, the anion uptake is likely guided by a positive patch in the otherwise negatively charged protein surface. The transient sodium release site in KR2 identified at Δt = 20 ms and created by a shift of the Arg^{243} (*15*) is located 5 Å away from the transient Cl^{354}-binding site in the triple water cluster (coordinated by the corresponding Arg^{223})

of *Nm*HR (fig. S22D), indicating that the sodium and chloride transport pathways may partially overlap on the extracellular side of the protein. Through consecutive steps driven by the charge of two arginine residues, the halide is proposed to arrive at an electrostatic molecular gate, a bottleneck in the anion uptake pathway. The gate likely opens upon interaction with the negative charge, allowing the anion to access the retinal-binding pocket. The subsequent closure of the electrostatic gate prevents anion backflow, imparting a directionality that is a characteristic feature of ion pumps. The counterparts of Arg^{95} and Asp^{231} forming the electrostatic gate in bacteriorhodopsin (Asp^{212} and Arg^{82}) play important functional roles as part of the complex counterion of the retinal and in the proton transfer pathway (*13*).

When comparing the proposed anion transport pathway of *Nm*HR with available archaeal HR structures, it becomes apparent that the anion-binding site coordinated by Gln^{105} identified in the *Hs*HR resting state (Asn^{92} in *Nm*HR) (*9*, *39*) does not align with the anion uptake pathway in *Nm*HR. Although in *Hs*HR, this anion-binding site is directly accessible from the bulk solvent, in *Nm*HR, the site is occluded from solvent by the extended N terminus and the different position of the B-C loop (fig. S22B). Conversely, the anion-binding site in the *Np*HR N state (*10*) is located over the retinal and in the proximity of Ile^{134} (Leu^{106} in *Nm*HR), ~4 Å away from Cl^{352} in *Nm*HR, indicating a plausible pathway toward the Cl^{353} site (fig. S22C). In addition, we observed how retinal isomerization increases the affinity for the anion in the transient Cl^{352}-binding site, allowing access to the cytoplasmic half of the protein and driving ion transfer (*40*–*42*); however, we have not found a clear conformational change switching the accessibility of the exit and uptake tunnel in the late photocycle, as has been proposed for *Np*HR (*10*, *16*). Although differences in the ion transport mechanism of archaeal and bacterial halorhodopsins may exist, the chloride pumps also share many commonalities. The large conformational changes in helix C of *Np*HR in the anion-free (O-like) state (*10*, *43*) and the existence of a salt bridge next to the resting-state chloride-binding site of the archaeal *Hs*HR and *Np*HR (*8*, *44*) suggest that the molecular gates may be a general feature of halorhodopsin ion pumps.

In summary, we have proposed the ion transfer pathway in bacterial halorhodopsin and discussed the interplay between the driving force created by the protein dipole moment and the control of transport by molecular gates. Furthermore, we have provided details about how light energy is converted into kinetic energy for chloride translocation. The resulting charge separation represents a fundamental feature for light energy conversion in nature as well as in technology.

REFERENCES AND NOTES

1. C. Miller, *Nature* **440**, 484–489 (2006).
2. A. Matsuno-Yagi, Y. Mukohata, *Biochem. Biophys. Res. Commun.* **78**, 237–243 (1977).
3. B. Schobert, J. K. Lanyi, *J. Biol. Chem.* **257**, 10306–10313 (1982).
4. C. Engelhard, I. Chizhov, F. Siebert, M. Engelhard, *Chem. Rev.* **118**, 10629–10645 (2018).
5. S. Yoshizawa *et al*., *Proc. Natl. Acad. Sci. U.S.A.* **111**, 6732–6737 (2014).
6. F. Zhang *et al*., *Nature* **446**, 633–639 (2007).
7. O. Jardetzky, *Nature* **211**, 969–970 (1966).
8. M. Kolbe, H. Besir, L.-O. Essen, D. Oesterhelt, *Science* **288**, 1390–1396 (2000).
9. W. Gmelin *et al*., *Photochem. Photobiol.* **83**, 369–377 (2007).
10. T. Kouyama, H. Kawaguchi, T. Nakanishi, H. Kubo, M. Murakami, *Biophys. J.* **108**, 2680–2690 (2015).
11. K. Kim *et al*., *Nat. Commun.* **7**, 12677 (2016).
12. T. Hosaka *et al*., *J. Biol. Chem.* **291**, 17488–17495 (2016).
13. E. Nango *et al*., *Science* **354**, 1552–1557 (2016).
14. K. Inoue *et al*., *Nat. Commun.* **4**, 1678 (2013).
15. P. Skopintsev *et al*., *Nature* **583**, 314–318 (2020).
16. I. Chizhov, M. Engelhard, *Biophys. J.* **81**, 1600–1612 (2001).
17. T. Tsukamoto, S. Yoshizawa, T. Kikukawa, M. Demura, Y. Sudo, *J. Phys. Chem. B* **121**, 2027–2038 (2017).
18. J. Tenboer *et al*., *Science* **346**, 1242–1246 (2014).
19. K. Pande *et al*., *Science* **352**, 725–729 (2016).
20. T. R. M. Barends *et al*., *Science* **350**, 445–450 (2015).
21. N. Coquelle *et al*., *Nat. Chem.* **10**, 31–37 (2018).
22. E. Claesson *et al*., *eLife* **9**, e53514 (2020).
23. P. Nogly *et al*., *Science* **361**, eaat0094 (2018).
24. P. Nogly *et al*., *Nat. Commun.* **7**, 12314 (2016).
25. G. Nass Kovacs *et al*., *Nat. Commun.* **10**, 3177 (2019).
26. T. Weinert *et al*., *Science* **365**, 61–65 (2019).
27. E. Prat *et al*., *Nat. Photonics* **14**, 748–754 (2020).
28. R. Efremov, V. I. Gordeliy, J. Heberle, G. Büldt, *Biophys. J.* **91**, 1441–1451 (2006).
29. J.-H. Yun *et al*., *Proc. Natl. Acad. Sci. U.S.A.* **118**, e2020486118 (2021).
30. A. Robertazzi, F. Krull, E.-W. Knapp, P. Gamez, *CrystEngComm* **13**, 3293–3300 (2011).
31. X. Lucas, A. Bauzá, A. Frontera, D. Quiñonero, *Chem. Sci.* **7**, 1038–1050 (2016).
32. S. Z. Borozan, M. V. Zlatović, S. Đ. Stojanović, *Eur. J. Biochem.* **21**, 357–368 (2016).
33. M. S. Smith *et al*., *ACS Chem. Biol.* **12**, 2535–2537 (2017).
34. C. Estarellas, A. Frontera, D. Quiñonero, P. M. Deyà, *Angew. Chem. Int. Ed.* **50**, 415–418 (2011).
35. L. M. Breberina, M. K. Milčić, M. R. Nikolić, S. Đ. Stojanović, *Eur. J. Biochem.* **20**, 475–485 (2015).
36. E. C. Law, H. R. Wilman, S. Kelm, J. Shi, C. M. Deane, *PLOS ONE* **11**, e0157553 (2016).
37. I. Gushchin *et al*., *Nat. Struct. Mol. Biol.* **22**, 390–395 (2015).
38. H. E. Kato *et al*., *Nature* **521**, 48–53 (2015).
39. M. Schreiner, R. Schlesinger, J. Heberle, H. H. Niemann, *J. Struct. Biol.* **190**, 373–378 (2015).
40. J. K. Lanyi, *FEBS Lett.* **175**, 337–342 (1984).
41. J. K. Lanyi, *FEBS Lett.* **464**, 103–107 (1999).
42. U. Haupts, J. Tittor, E. Bamberg, D. Oesterhelt, *Biochemistry* **36**, 2–7 (1997).
43. S. Kanada, Y. Takeguchi, M. Murakami, K. Ihara, T. Kouyama, *J. Mol. Biol.* **413**, 162–176 (2011).
44. T. Kouyama *et al*., *J. Mol. Biol.* **396**, 564–579 (2010).
45. S. Mous *et al*., SFX raw data for: Dynamics and mechanism of a light-driven chloride pump, PSI Public Data Repository (2022); https://doi.org/doi.psi.ch/detail/10.16907/8ecae5fe-4c00-4d59-be3d-5274f06188c2.
46. S. Mous *et al*., SSX raw data for: Dynamics and mechanism of a light-driven chloride pump, PSI Public Data Repository (2022); https://doi.org/doi.psi.ch/detail/10.16907/12079b73-6563-467a-890a-2ab43e678343.
47. S. Mous *et al*., 13.7 keV anomalous data for: Dynamics and mechanism of a light-driven chloride pump, PSI Public Data Repository (2022); https://doi.org/doi.psi.ch/detail/10.16907/14c30658-cc0b-41fe-b25b-240a9790d5ec.

ACKNOWLEDGMENTS

We thank the Macromolecular Crystallography group for support during the testing of crystals at the Swiss Light Source and the access and support of the Crystallization Facility at Swiss Light Source; the Paul Scherrer Institute, Villigen, Switzerland, for provision of XFEL and synchrotron radiation beamtime at beamlines X06SA (PXI) of the Swiss Light Source and Alvra at SwissFEL; everybody involved in ensuring the smooth operation of the SwissFEL X-ray Free Electron Laser and Swiss Light Source during our experiments; and F. Allain, S. Jonas, and A. Gossert for access to the office, laboratory space, and equipment at L floor of HPP building of ETH Zurich and for the supportive working environment provided. **Funding:** This work was supported by the Swiss National Science Foundation (Ambizione grant PZ00P3_174169 to P.N.; project grant 31003A_179351 to J.S.; and project grant 310030B_173335 to G.F.X.S.); the National Centre of Competence in Research: Molecular Ultrafast Science and Technology (C.M. and J.S.); the German Research Foundation via SFB 1078, projects B3 (J.H.), C6 (I.S.) and via EXC 2008/1 UniSysCat 390540038 (J.H.); Holcim Stiftung (P.M.); European Union's Horizon 2020 research and innovation program (Marie-Sklodowska-Curie grant agreements 701646 and 701647 to G.G., D.K., and S.B.); and the European Research Council (ERC) European Union's Horizon 2020 research and innovation program (grant 678169 'PhotoMutant' to I.S.). **Author contributions:** P.N. designed and coordinated the project. I.S. and S.S. coordinated quantum chemical calculations. C.M. coordinated the pump-probe experiments at the Alvra endstation. J.H. coordinated time-resolved spectroscopy. G.F.X.S. coordinated and supported crystallographic applications at SwissFEL and contributed to discussions throughout the project. S.M. expressed, purified, and crystallized *Nm*HR. S.M., A.F., D.K., and P.M. secured a constant supply of sample during the SFX beamtime. S.M. and D.J. optimized crystal injection. D.J., G.G., F.D., I.M., D.G., and P.S. operated and aligned the lipidic cubic phase injector during the beamtime. P.J., M.J., K.N., G.K., C.C., C.A., M.J., and C.M. aligned and operated the endstation, including the laser system, and designed the Alvra prime pump-probe station. D.O. and K.N. built and operated the SFX data analysis pipeline. T.W., C.M.C., and S.B. performed data processing during the beamtime. S.B., J.S., V.P., and M.W. recorded progress during data collection. J.S. supported P.N. in coordination of the experiment at SwissFEL. S.M. and P.N. optimized data processing. S.M., G.G., and P.N. refined and interpreted structures. S.S. and I.S. performed quantum-chemical calculations. D.E. and S.M. performed the time-resolved spectroscopic experiments and interpreted them together with J.H. E.P. synchronized diode and detector triggering at the synchrotron. D.J., F.D., and T.W. built the pump-probe setup at the synchrotron. S.M., G.G., P.N., and D.J. collected synchrotron data with suggestions on anomalous data collection and analysis from T.W. P.N. wrote the manuscript with direct contributions from S.M., G.G., D.E., J.H., S.S., and I.S. with further suggestions from most of the other authors. All authors read and approved the manuscript. **Competing interests:** The authors declare no competing interests. **Data and materials availability:** Resting-state coordinates and structure factors have been deposited in the PDB database under accession codes 708F (SFX), 708L (SSX), and 708Y (13.7 keV anomalous data). For the light-activated datasets, coordinates, light amplitudes, dark amplitudes, and extrapolated structure factors have been deposited in the PDB database under accession codes 708G (10 ps), 708H (10 ns), 708I (1 µs), 708J (20 µs), 708K (300 µs), 708M (2.5 ms), 708N (7.5 ms), 708O (12.5 ms), 708P (17.5 ms), 708Q (22.5 ms), 708R (27.5 ms), 708S (32.5 ms), 708T (37.5 ms), 708U (45 ms), 708V (55 ms), and 708Z (photostationary; 13.7 keV anomalous data). SFX raw data (*45*), SSX raw data (*46*), and 13.7 keV anomalous data (*47*) are available at the PSI Public Data Repository.

SUPPLEMENTARY MATERIALS

science.org/doi/10.1126/science.abj6663
Materials and Methods
Supplementary Text S1 to S3
Figs. S1 to S29
Tables S1 to S13
References (*48*–*81*)
Movie S1
MDAR Reproducibility Checklist

View/request a protocol for this paper from *Bio-protocol*.

29 May 2021; accepted 26 January 2022
Published online 3 February 2022
10.1126/science.abj6663